Bone infection site targeting nanoparticle-antibiotics delivery vehicle to enhance treatment efficacy of orthopedic implant related infection

Bin'en Nie [a,1], Shicheng Huo [a,1], Xinhua Qu [a,1], Jingjing Guo [b], Xi Liu [c], Qimin Hong [a], You Wang [a], Jianping Yang [b], Bing Yue [a,*]

[a] Department of Bone and Joint Surgery, Department of Orthopedics, Renji Hospital, School of Medicine, Shanghai Jiaotong University, Shanghai, 200127, China
[b] State Key Laboratory for Modification of Chemical Fibers and Polymer Materials, College of Materials Science and Engineering, Donghua University, Shanghai, 201620, China
[c] Key Laboratory of Carcinogenesis and Translational Research (Ministry of Education) Department of Radiology, Peking University Cancer Hospital & Institute, Beijing, 100142, China

ARTICLE INFO

ABSTRACT

Orthopedic implants account for 99% of orthopedic surgeries, however, orthopedic implant-related infection is one of the most serious complications owing to the potential for limb-threatening sequelae and mortality. Current antibiotic treatments still lack the capacity to target bone infection sites, thereby resulting in unsatisfactory therapeutic effects. Here, the bone infection site targeting efficacy of D6 and UBI$_{29-41}$ peptides was investigated, and bone-and-bacteria dual-targeted nanoparticles (NPs) with D6 and UBI$_{29-41}$ peptides were first fabricated to target bone infection site and control the release of vancomycin in bone infection site. The results of this study demonstrated that the bone-and-bacteria dual-targeted mesoporous silica NPs exhibit excellent bone and bacteria targeting efficacy, excellent biocompatibility and effective antibacterial properties in vitro. Furthermore, in a rat model of orthopedic implant-related infection with methicillin-resistant *Staphylococcus aureus*, the growth of bacteria was evidently inhibited without cytotoxicity, thus realizing the early treatment of implant-related infection. Hence, the bone-and-bacteria dual-targeted molecule-modified NPs may target bacteria-infected bone sites and act as ideal candidates for the therapy of orthopedic implant-related infections.

1. Introduction

Orthopedic implant-related infection (OII) is a catastrophic complication after orthopedic surgery that can lead to the failure of the operation, joint deformity, amputation, or death. It has become a global challenge with an enormous economic burden on public health systems [1–3]. Unfortunately, there is currently no gold standard for the therapy of orthopedic implant-related infections. Antibiotic therapy continues to play a vital role in the clinical treatment of orthopedic implant-related infections, usually involving systemic or local antibiotic therapy at high doses over a prolonged period [4,5]. However, the current antibiotic therapy is still far from satisfactory, with treatment failure rates of approximately 20% [6]. There are various reasons for such high rates. First, clinical biochemical examinations, joint fluid analysis, and imaging investigations fail to diagnose orthopedic implant-related infections at an early stage, leading to improper treatment, treatment delay, and even no treatment [7–9]. Second, bone tissue has biological specificities, such as low blood flow, high density, and poor permeability, which result in poor penetration of antibiotics into the bone. Third, the infection sites cannot be located, which leads to blindness in the treatment.

Furthermore, orthopedic implant-related infections are often accompanied by the formation of bacterial biofilms that become resistant to antibiotics, thereby resulting in prolonged infection [10,11]. In addition, systemic exposure to high-dose antibiotics can cause severe toxicities and adverse effects, such as hepatic and renal toxicity [12,13].

Traditional antibiotics still suffer from issues of efficacy and feasibility [14,15]. They are not able to target bone infection sites and are unsuccessful at the biofilm, resulting in unsatisfactory therapeutic effects. Several strategies were being developed to counteract the crisis of antibiotic resistance, including antibiotic-strengthening and antibiotic-free strategy, such as phototherapy and photo-assisted antibiotics. However, such strategies are only viable for subcutaneous tumors and wound infections and are thus unsuitable for treating deep infections [16,17]. Therefore, it is an urgent need to invent a novel therapeutic approach to enhance the antibacterial efficacy. Nanotechnology has gained tremendous interest in antibacterial applications owing to its intrinsic antibacterial activity, targeted delivery, and reduced opportunities for resistance development [18–21]. Yang et al. synthesized bacteria-targeted peptide-functionalized mesoporous silica nanoparticles (MSNs) for delivery of gentamicin to the infection site to enhance the antibacterial activity of intracellular pathogens and eliminate inflammation caused by bacteria [22]. Furthermore, silicon nanoparticles (NPs) can be modified with cyclic 9-amino-acid peptide to target *Staphylococcus aureus* and control the release of vancomycin to enhance antibacterial efficacy [23]. For bone infection, the targeted delivery of antibiotics to the bone tissue can improve the bone penetration, which may result in improved activity against bacteria in bone tissue [24]. Although bacteria- or bone-targeted NPs have been widely investigated for the targeted delivery of antibiotics to the infection site or bone site, these studies simply targeted soft tissue infection sites or bone sites and lacked specific targeting to the infected bone. This results in poor penetration of antibiotics into the bone infection site and poor treatment outcomes.

Bone targeting and bacterial targeting had been widely investigated in the bone disease such as bone tumor, bone infection. Among that Peptide D_6, synthesized by Kasug in 2000, is an effective bone-targeted drug carrier molecule, due to aspartic acid have high affinity with bone tissue [25–28]. Peptide UBI_{29-41} is the most commonly used bacteria-targeted agent with six positively charged residues, which could result in better targeting capability duo to higher negative charge of *S. aureus* [29]. Studies have shown that UBI_{29-41} show 100% sensitivity and 88% specificity for vertebral osteomyelitis [30]. Other studies have demonstrated that UBI_{29-41} can distinguish between infection and aseptic loosening around the prosthesis [31]. Therefore, UBI_{29-41} peptides are promising for clinical applications in locating infected lesions.

In this study, we developed a bone-and-bacteria dual-targeted MSN approach to achieve targeted delivery of vancomycin to the bone infection site and improve the therapeutic efficacy of orthopedic implant-related infection. We investigated the bone infection site targeting efficacy of D6 and UBI_{29-41}, which could target bone and bacteria, respectively. Moreover, bone-and-bacteria dual-targeted MSNs were fabricated to target the delivery of vancomycin to the bone infection site, and the antimicrobial activity of dual-targeted MSN in vitro against methicillin-resistant *Staphylococcus aureus (MRSA)* was investigated to evaluate its antibacterial efficacy in an animal model of orthopedic implant-related infection.

2. Materials and methods

2.1. Materials

The chemicals used in the experiments, including tetraethyl orthosilicate (TEOS), 3-aminopropyltriethoxysilane (APTES), hexadecyl trimethyl ammonium bromide (CTAB, 25 wt% in H_2O), 1-ethyl-3(3-(dimethylamino) propyl) carbodiimide (EDC), N-hydroxysuccinimide (NHS), Fe(acac)3, sodium citrate ($Na_3C_6H_5O_7 \cdot 2H_2O$), and all organic

chemicals, were obtained from Sigma-Aldrich Trading Co., Ltd. (Shanghai, China). COOH-PEG-COOH (MW = 4KD, Seebio, Shanghai), The D_6 peptide, UBI_{29-41} peptide, PEG-D6 and PEG-UBI_{29-41} were synthesized by GL Biochem (Shanghai, China), and their characterization results are presented in Figs. S1–S6. Fetal bovine serum, penicillin-streptomycin, trypsin, and α-MEM were obtained from Gibco Life Technologies Co. (NY, USA). The LIVE/DEAD BacLight Bacterial Viability kit (Thermo Fisher). All chemicals were of analytical grade and were not further purified.

2.2. Methods

2.2.1. Surface functionalize MSN with PEG-D_6 and PEG-UBI_{29-41}

Synthesis of MSN: 6.0 g CTAB and 0.16g triethanolamine was dissolved in 60 mL Deionized water (DI water) at 80 °C and stirred for 1h, then dropwise added the mixed solution of 16 mL cyclohexane and 4.0 mL TEOS. After reacting at 60 °C for 8h, the mixture was repeatedly purified by centrifugation and washed with ethanol and DI water. Afterward, the MSNs were dispersed in ethanol containing 12 M HCl and stirred at 50 °C for 12 h to remove CTAB. The synthesized monodisperse silica was collected by centrifugation, washed with ethanol, and dried under vacuum at 37 °C for 12 h.

MSNs surface amination: The MSNs were modified with amine-containing silane APTES. Briefly, 1 g MSNs were added to 100 mL toluene then added 1 mL APTES, and the mixture was refluxed at 80 °C for 20 h, followed by centrifugation at 11000 rpm for 15 min. Subsequently, it was centrifuged and washed with absolute ethanol at 11000 rpm for 15 min and lyophilized for 36 h to obtain MSN-NH_2 powder.

Activation of the carboxyl group: (1) Activation of bone-targeted polyethylene glycol: 9.6 mg EDC, 5.8 mg NHS, and 1 mg -COOH-PEG-D_6 were added to PBS (0.2 M, pH = 6.1) and stirred at room temperature (RT) for 30 min to activate the carboxyl group. (2) Activation of bacteria-targeted Polyethylene Glycol: 9.6 mg EDC, 5.8 mg NHS, and 1 mg -COOH-PEG-UBI_{29-41} was added to PBS (0.2 M, pH = 6.1) and stirred at RT for 30 min to activate the carboxyl group. (3) Activation of bone-targeted and bacteria-targeted polyethylene glycol: 9.6 mg EDC, 5.8 mg NHS, 0.5 mg -COOH-PEG-D_6, and 0.5 mg -COOH-PEG-UBI_{29-41} were added to PBS (0.2 M, pH = 6.1) and stirred at RT for 30 min to activate the carboxyl group.

Amidation reaction: Mixed 100 mg MSN-NH_2 with 40 mL PBS (pH = 7.4) and the above solution were added after carboxyl activation. After adjusting the pH to neutral, the solution was stirred at RT for 12 h. Afterward, it was subjected to repeated centrifugation and washing with distilled water at 11000 rpm to obtain bone-targeted MSN (MSN@D), bacteria-targeted MSN (MSN@UBI), and dual-targeted (bone-targeted and bacteria-targeted) MSNs (MSN@D&U). The obtained powder was lyophilized and stored at 4 °C. To obtain FITC-labeled MSNs, MSNs were mixed with 2 mL of FITC aqueous solution (1 mg/mL). After being shaken under dark conditions for 24 h at 37 °C to reach equilibrium, the FITC-loaded MSNs were collected via centrifugation.

Characterization: The morphology of the NPs was examined by scanning electron microscope (SEM, Hitachi, Japan) and transmission electron microscopy (TEM, Hitachi, Japan). The BET surface area and pore size of MSNs was characterized by nitrogen adsorption-desorption using BET and Barret-Joyner-Halenda model analysis. The chemical states of the NPs were analyzed by fourier transform infrared spectroscopy (FTIR, Thermo Fisher Scientific, USA) and X-ray diffraction (XRD, Bruker, USA). The zeta potential of the NP suspension was measured using a Nanosize & Zeta Potential Analyzer (Litesizer 500, Austria).

2.2.2. Drug loading and in vitro release

Vancomycin loading into MSNs: Vancomycin loading into MSN was performed following an impregnation approach. Vancomycin and MSNs (MSNs, MSN@D, MSN@UBI, or MSN@D&U) were added to PBS (pH 7.4) at a weight ratio of 1:1 and stirred for 16 h at room temperature (RT). After repeated centrifugation and washing, the supernatant was

collected and recorded for absorption at 280 nm to quantify free vancomycin. The encapsulation efficiency and loading capacity were calculated as follows: encapsulation efficiency (%, w/w) = (feed drug content - free drug content)/feed drug content × 100%; loading capacity (%, w/w) = (feed drug content - free drug content)/(feed drug content + NP content - free drug content) × 100%.

Vancomycin release assays from MSNs in vitro: 10 mg of loaded MSN material was dispersed in 5 mL PBS buffer solution (pH = 7.4), sonicated for 10 min, and transferred to a dialysis bag (12 kDa molecular weight cutoff) that allowed only vancomycin diffusion. At specific time points (2h, 4h, 6h, 12h, 24h, 72h, 120h, and 168 h), the solution was collected for further analysis and replaced with fresh medium. The absorbance at a wavelength of 280 nm was measured using a UV–Vis spectrophotometer (Shimadzu UV-2600).

2.2.3. HA (Hydroxyapatite) binding capability and bacterial affinity

In vitro HA binding evaluation: HA binding capability was measured as described in previous reports [32]. In brief, 50 µg mL^{-1} FITC-labeled MSNs in 20 mL DI water containing HA (0.75 mg mL^{-1}) was stirred at 550 rpm at 37 °C for 4 h. At the predetermined time point, an aliquot of 200 µL was diluted with 1.0 mL DI water and centrifuged at 1000×g for 5 min to remove the HA and bound MSNs. The MSNs concentration in the supernatant was quantified by measuring FITC fluorescence intensity. Bound MSNs were calculated by subtracting the unbound MSNs from the total MSNs.

Bacterial affinity studies: The targeting capability of MSNs in vitro was investigated using *MRSA* (ATCC 43300). Bacteria were allowed to grow in Mueller-Hinton broth (MHB) at 37 °C for 12 h in an incubator shaker at 250 rpm. Subsequently, the mid-log phase suspension of *MRSA* cells was incubated with MSN material (10 µg mL^{-1}) at 37 °C for 30 min with gentle stirring for 2 h. Afterward, the mixture was centrifuged at 4000×g for 10 min, and the bacteria pellets were fixed with 2.5% glutaraldehyde. SEM observations and chemical analyses were carried out using a Hitachi S4800 equipped with a Kevex Sigma energy dispersive spectrometer (EDS). The bacterial affinity of the MSNs was further explored using flow cytometry. Briefly, *MRSA* suspensions were incubated with FITC-labeled NPs (10 µg mL^{-1}) for 30 min at 37 °C. Finally, the localization of the materials on the bacteria was quantified by flow cytometry.

2.2.4. In vitro antibacterial assay

Determination of the MIC: The MICs against *MRSA* were investigated as previously described [33], bacteria in the logarithmic phase of growth were diluted to 1 × 10^6 CFU mL^{-1} in MHB medium. Thereafter, a two-fold dilution series of NPs, from 1024 µg mL^{-1} to 1 µg mL^{-1}, were prepared and plated in a volume of 100 µL in 96-well plates. Bacterial suspensions (100 µL) were added to each well. The plates were incubated for 18 h at 37 °C, and the MIC was determined as the lowest concentration that resulted in complete growth inhibition.

Time kill assay: The growth curves of *MRSA* were recorded using a SPARK 10 M microplate reader (TECAN, Switzerland) to evaluate the antibacterial properties of the NPs. Briefly, the bacteria were diluted to approximately 10^6 CFU mL^{-1} after reaching the logarithmic phase and supplemented with MICs of NPs with a total volume of 500 µL in each well of a 48-well plate. Subsequently, the 48-well plate was loaded into a microplate reader for continuous culture at 37 °C to obtain growth curves. The absorbance at 600 nm in each well was monitored every 1h for 12 h. The culture medium was used as a negative control, and the bacterial suspension without the MSNs was defined as a positive control.

Morphological characterization of bacteria: *MRSA* (10^6 CFU mL^{-1}) was incubated with MSN material at 37 °C for 6 h. After treatment, bacterias were collected by centrifugation at 5000 rpm for 10 min and fixed with 2.5% glutaraldehyde overnight at 4 °C. Afterward, the samples were dehydrated, freeze-dried, and sputter-coated with platinum, as described above. Finally, the samples were observed using SEM.

Biofilm inhibition assay: Ti discs were placed into the wells of a 24-well cell culture plate. Thereafter, 1 mL of bacterial culture (10^6 CFU mL^{-1}) containing MSNs@V or vancomycin at their respective MICs was added and incubated at 37 °C for 18 h. At the desired time point, planktonic cells were removed from the Ti substrate by washing twice with sterile PBS solution. For CLSM, the biofilms on the Ti substrate were stained with the LIVE/DEAD BacLight Bacterial Viability kit according to the manufacturer's instructions.

In addition, the biofilms were stained with 1% crystal violet for 15 min. The Ti discs were rinsed twice with DI water and solubilized with 96% ethanol. The optical density at 595 nm was determined as a measure of biofilm mass using a microtiter plate reader. The *anti*-biofilm properties of each MSN@V were further evaluated by SEM, and further processing of the samples was performed as described above.

2.2.5. Cell cytotoxicity, morphology and hemolytic activity of MSN

Rat bone marrow mesenchymal stem cells (rBMSCs) were isolated and expanded as described in previous study [34]. The third generation of rBMSCs was used in the experiments.

Cytotoxicity assay: The cytotoxicity of the MSNs was evaluated using the Cell Counting Kit-8. Briefly, rBMSCs were seeded in a 96-well plate for 24 h in a standard cell culture atmosphere. Subsequently, different samples with concentrations of 0–1000 µg mL^{-1} were added to 96-well plates plated with rBMSCs for another 1, 3, or 5 d. At the predetermined time points, 90 µL fresh cell culture medium and 10 µL CCK-8 solution were added to each well and incubated for an additional 2 h. The absorbance at 450 nm was detected using a spectrophotometer. Each measurement was performed on three distinct samples, repeated in triplicate. Then the live/dead staining kit (Dojindo, Japan) was used to evaluate cell viability. The cells were treated with different MSNs (64 µg mL^{-1}) for 24 h. The samples were stained with calcein acetoxymethyl ester and propidium iodide for 15 min at 37 °C away from light. Images were observed using a fluorescence microscope (Nikon, Japan).

Morphological assessment of cells: Rhodamine phalloidin (Invitrogen) were used to analyze the cell morphology and cytoskeleton. Briefly, cells were co-cultured with MSNs (64 µg mL^{-1}) for 24h, then the cells were fixed in 4% paraformaldehyde for 30 min, washed three times with PBS, and permeabilized with 0.25% Triton X-100 at room temperature for 30 min. Thereupon, F-actin was stained with rhodamine phalloidin for 30 min in the dark, and 4,6-diamidino-2-phenylindole (DAPI) was added to stain the nuclei. The images of the samples were observed using CLSM.

Hemolytic activity: The hemolytic activities of MSNs were determined by hemolysis of rat erythrocytes. Fresh rat blood was obtained from anesthetized rats by cardiac puncture into syringes containing 3.8% sodium citrate as an anticoagulant. The red blood cells were subsequently washed three times with 25 mL of PBS and centrifuged at 116×g for 5 min at 4 °C. The cell pellets were resuspended in a 4% (v/v) red blood cell suspension with prechilled PBS, and 100 µL was added to each well of the 96-well plates. Afterward, a two-fold dilution series of MSNs, from 512 µg mL^{-1} to 2 µg mL^{-1}, was added to each well to reach a final volume of 200 µL. After 1 h of incubation at 37 °C, the plate was centrifuged and the supernatant were transferred to a new 96-well microplate. The release of hemoglobin was determined by measuring the absorbance of the supernatant at 414 nm. For calibration, 0% and 100% hemolysis were determined in PBS and 0.1% (v/v) Triton X-100, respectively.

2.2.6. In vivo therapy and histochemistry analysis

All animal experiments were approved by the Animal Ethics Committee of Shanghai Rat&Mouse Biotech Co.,Ltd (Ethic ID: 2020R016) and were conducted in compliance with all relevant ethical regulations for animal testing and research. Three-month-old female Sprague Dawley (SD) rats, obtained from Shanghai Rat&Mouse Biotech Co.,Ltd, were used for surgical intramedullary implantation. The Ti implant (1.5 mm in diameter and 15 mm in length) was contaminated with *MRSA*

(10^6 CFU mL^{-1}) and were implanted in the left femurs via the femoral condyles. The rats were housed in ventilated cages on corn bedding and provided with water and chow ad libitum (six rats in each group). Over the course of 1 d after orthopedic implant surgery, saline, MSNs (10 mg kg^{-1}), or vancomycin (10 mg kg^{-1}) were intravenously injected. After 3 weeks, the rats were sacrificed by cervical dislocation.

Evaluation of gross bone pathology and radiology: The cortical bone destruction of rats was examined with X-ray after 3 weeks. The radiographic scores were calculated as described in previous studies (N = 5) [35,36]. Five rats per group were sacrificed 3 weeks after surgery, and the femurs were dissected to evaluate the gross bone pathology

according to the aforementioned criteria. In addition, the femurs were scanned using a micro-CT scanner (SkyScan 1072; Bruker). Trabecular morphometry was characterized by analyzing the BV/TV and Tb. Th and Tb. Sp.

Quantitative determination of MRSA: Briefly, animals were sacrificed, the Ti implant were removed, and the surrounding bone tissue was ground under a sterile environment after 3 weeks (N = 5). The Ti implants were detached by sonication, and the bones were crushed in PBS. The number of bacteria on Ti implants and surrounding bone tissue was determined by plating serial dilutions. Furthermore, CLSM and SEM were used to determine the bacterial colonization on Ti implants in vivo.
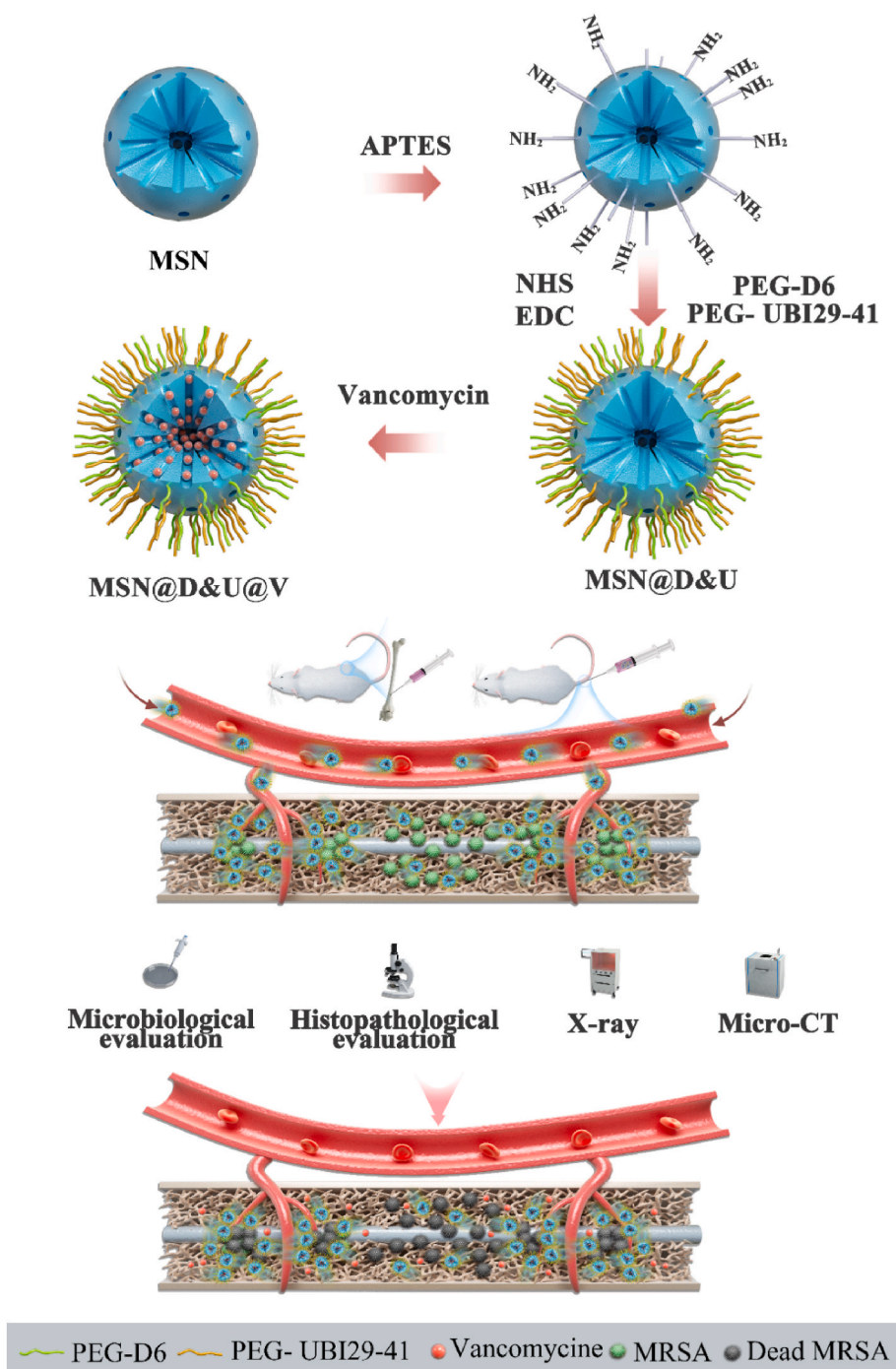
Scheme 1. Synthesis of mesoporous silica nanoparticles (MSNs) with dual targeting (bone targeting and bacteria targeting) and investigation of their biofunction in vitro and in vivo. Then we evaluated the antimicrobial activity of dual-targeted MSN in vitro against methicillin-resistant *Staphylococcus aureus (MRSA)* and investigated its antibacterial efficacy in an animal model of implant-related infection.

Evaluate the histopathology of the bone tissue around the Ti implant: Dissected femurs were decalcified with 10% EDTA for 4 weeks and subjected to histological analysis using H&E staining and Gram staining according to a previously described method [37]. Bone histomorphometry was performed using optical microscopy. To evaluate the biosafety of MSNs, the major organs of the rats were stained with H&E.

2.3. Statistical analysis

All experiments were performed using biological replicates, and the data are expressed as the mean $\pm$ standard deviation. One-way analysis of variance (ANOVA) was used to analyze the significant differences between samples. P values $<$ 0.05 were considered to indicate statistically significant results.

3. Results and discussion

3.1. Bone infection site targeting efficacy with D6 and UBI$_{29-41}$ modified nanoparticles

D6 and UBI$_{29-41}$ peptides exhibit excellent bone- and bacteria-targeting ability, respectively, and have been widely used to modify NPs for the targeted delivery of drugs to bone or to trace bacteria and improve the therapeutic efficacy of bone diseases such as bone tumors and osteoporosis [27,38,39]. However, for bone infection, bone-targeted NPs deliver antibiotic vehicles lacking bacterial targeting, and the bacteria-targeted NPs deliver antibiotic vehicles lacking bone targeting. In this study, we investigated the bone infection site targeting efficacy of bone-and-bacteria dual-targeted MSN modified with D6 and UBI$_{29-41}$ peptides, further, the therapeutic efficacy of orthopedic implant-related infection with dual-targeted MSN loading vancomycin was also investigated (Scheme 1).

Fe$_3$O$_4$ NPs were used to characterize the targeting efficacy on bone infection sites of D6 and UBI$_{29-41}$ peptides. The characterization results of Fe$_3$O$_4$ nanospheres were demonstrated in Fig. S7 and Fe$_3$O$_4$ NPs possessed good biocompatibility (Fig. S8).

As shown in Fig. 1a, PEG-D$_6$- or PEG-D$_6$ and PEG-UBI$_{29-41}$-modified Fe$_3$O$_4$ NPs (Fe$_3$O$_4$@D and Fe$_3$O$_4$@D&U) exhibited stronger binding with HA in contrast to UBI$_{29-41}$-modified Fe$_3$O$_4$ NPs (Fe$_3$O$_4$@UBI). In addition, it was confirmed that the FITC fluorescence intensity was linearly correlated with NP concentration (Fig. 1b). The results suggested that PEG-D$_6$-or PEG-D$_6$ and PEG-UBI$_{29-41}$-modified NPs showed enhanced bone-targeting capacity. Subsequently, we investigated the affinity of Fe$_3$O$_4$ NPs for bacteria in vitro. The flow cytometry results demonstrated that PEG-UBI$_{29-41}$- or PEG-D$_6$ and PEG-UBI$_{29-41}$-modified NPs showed enhanced bacterial affinity (Fig. 1c and d), thereby confirming the dual targeting of the NPs.

Moreover, the magnetic resonance imaging (MRI) contrast performance of Fe$_3$O$_4$ NPs was characterized. Fig. 1e shows the T2WI images of the NP (including Fe$_3$O$_4$@SiO$_2$, Fe$_3$O$_4$@D, Fe$_3$O$_4$@UBI, and Fe$_3$O$_4$@D&U) phantoms at various concentrations by a 7T MRI scanner. To evaluate the potential of Fe$_3$O$_4$ NPs as diagnostic MRI contrast agents, the T2 signal intensity (SI) of Fe$_3$O$_4$ NP phantoms at various concentrations were measured. As shown in Fe$_3$O$_4$, the T2 SI revealed a concentration-dependent darkening effect and decreased significantly with increasing concentration for the four kinds of Fe$_3$O$_4$ NPs. Moreover, the T2 SI of the Fe$_3$O$_4$@D&U phantom was higher compared to the other Fe$_3$O$_4$ NP phantoms at the same concentration. In addition, the results showed strong linear relationships between the T2 relaxation rates (1/T2) and Fe$_3$O$_4$ NP concentrations (Fe$_3$O$_4$@SiO$_2$: $R^2 = 0.969$, Fe$_3$O$_4$@D: $R^2 = 0.988$, Fe$_3$O$_4$@UBI: $R^2 = 0.978$, Fe$_3$O$_4$@D&U: $R^2 = 0.990$) (Fig. 1f), suggesting Fe$_3$O$_4$ NPs as suitable contrast agents for MRI.

The preliminary results of the Fe$_3$O$_4$ NPs in vitro enabled the accurate evaluation in vivo. The four groups of bacteria-bearing rats were examined using a 7T MRI scanner at an early stage of infection (3 d after the bacterial infection), and matched T2WI images were acquired before

and 30 min after the intravenous administration of Fe$_3$O$_4$ NPs. As shown in Fig. 1g, the T2 SI of the infected left femur of rats significantly decreased in all the groups after injection, while the signal dropping of Fe$_3$O$_4$@D&U-treated rats was more remarkable compared to the other Fe$_3$O$_4$ NP groups. As shown in Fig. 1h, within the Fe$_3$O$_4$ NP subgroups, the T2-post/T2-pre SI of the infected left femur of rats gradually decreased in the Fe$_3$O$_4$@SiO$_2$, Fe$_3$O$_4$@D, Fe$_3$O$_4$@UBI, and Fe$_3$O$_4$@D&U. After 30 min of injection, rats were sacrificed, and the left femurs and organs (heart, liver, spleen, lung, and kidney) were obtained to measure the Fe concentrations. As shown in Fig. 1i, the Fe concentrations were significantly increased in the left femurs of Fe$_3$O$_4$@D&U-treated rats compared to other groups, showing a higher NP accumulation in bone infection site. In addition, Fig. S9 displays the histopathological studies of the major organs of the rats after MRI testing in vivo. As expected, no agglomerated particles and no signs of organ damage were observed in the organs, suggesting that the Fe$_3$O$_4$ NPs did not cause histological toxicity to the main organs of rats. Therefore, bone-and-bacteria dual-targeted NPs could effectively target the bone infection site.

3.2. Synthesis of MSN and surface functionalize MSN with PEG-D$_6$ and PEG-UBI$_{29-41}$

The targeted delivery of drugs to the disease site plays a critical role in enhancing the disease treatment efficacy [40]. Based on the excellent bone infection site targeting effect of D6-and UBI$_{29-41}$-modified NPs, we synthesized D6-and UBI$_{29-41}$-modified MSNs to target the delivery of vancomycin to the bone infection site. MSNs have been extensively employed as drug delivery systems because of their advantages, including ultrahigh specific surface area, large pore volume, ease of surface modification, ordered mesoporous structure, uniform, adjustable, and tunable pore size, and excellent biocompatibility [41,42]. The morphologies of MSN, MSN@D (PEG-D6-modified MSN), MSN@UBI (PEG-UBI$_{29-41}$-modified MSN), and MSN@D&U (PEG-D6 and PEG-UBI$_{29-41}$-modified MSNs) were characterized by scanning electron microscopy (SEM) and transmission electron microscopy (TEM). As shown in Fig. 2a, the MSN materials had uniform spherical particles with a size of approximately 100 nm. Additionally, TEM images confirmed that the MSN materials had excellent dispersity, uniform size distribution, and a highly ordered mesoporous structure (Fig. 2b). Fourier-transform infrared (FTIR) spectroscopy was used to confirm the successful preparation of bone-and-bacteria dual-targeted MSNs (Fig. 2c). The characteristic peak at 1082 cm^{-1} was assigned to the stretching vibration of O–Si–O, and the characteristic peak at 799 cm^{-1} was assigned to the symmetric stretching vibration of Si–OH. The CH stretching modes of the methyl and methylene groups of the polymer chain corresponding to the PEG vibration spectrum were between 2980 cm^{-1} and 2880 cm^{-1}. The PEGylated structure was confirmed at 2934 cm^{-1}, which was attributed to the C- of linear PEG. The asymmetric stretching vibration of CH$_2$ at 1460 cm^{-1} is attributed to the asymmetric bending vibration of –N(CH$_3$)$_3^+$, which coincides with the spectrum of pure MSNs. It was not found in the spectrum of pure MSN, but the 1654 cm^{-1} peak in the spectrum was observed in MSN@D, MSN@UBI$_2$, and MSN@D&U, which was confirmed to be the –NH bend and –CN of the amide stretch, confirming the successful formation of amide bonds. The N$_2$ adsorption-desorption isotherms of MSN exhibited type IV isotherm characteristics, indicating a mesoporous structure and a narrower size distribution of MSNs (Fig. 2d and e). The corresponding pore volume, Brunauer-Emmett-Teller (BET) surface area, and mesopore size were calculated to be 1.63 cm^3 g^{-1}, 414.88 m^2 g^{-1}, and 3.49 nm, respectively.

MSNs are highly polar owing to the large amount of Si–OH on the surface and the zeta potential, which is −20.9 mV (Fig. 2f). MSN was functionalized with amino groups by a silane coupling agent to endow a positive charge on MSNs, and the zeta potential of the obtained MSN-NH$_2$ was +26.7 mV. However, the zeta potential of MSN@D dropped to +21.9 mV. This phenomenon may result from –COOH PEGylation, which increases the negative charge, thereby reducing the zeta
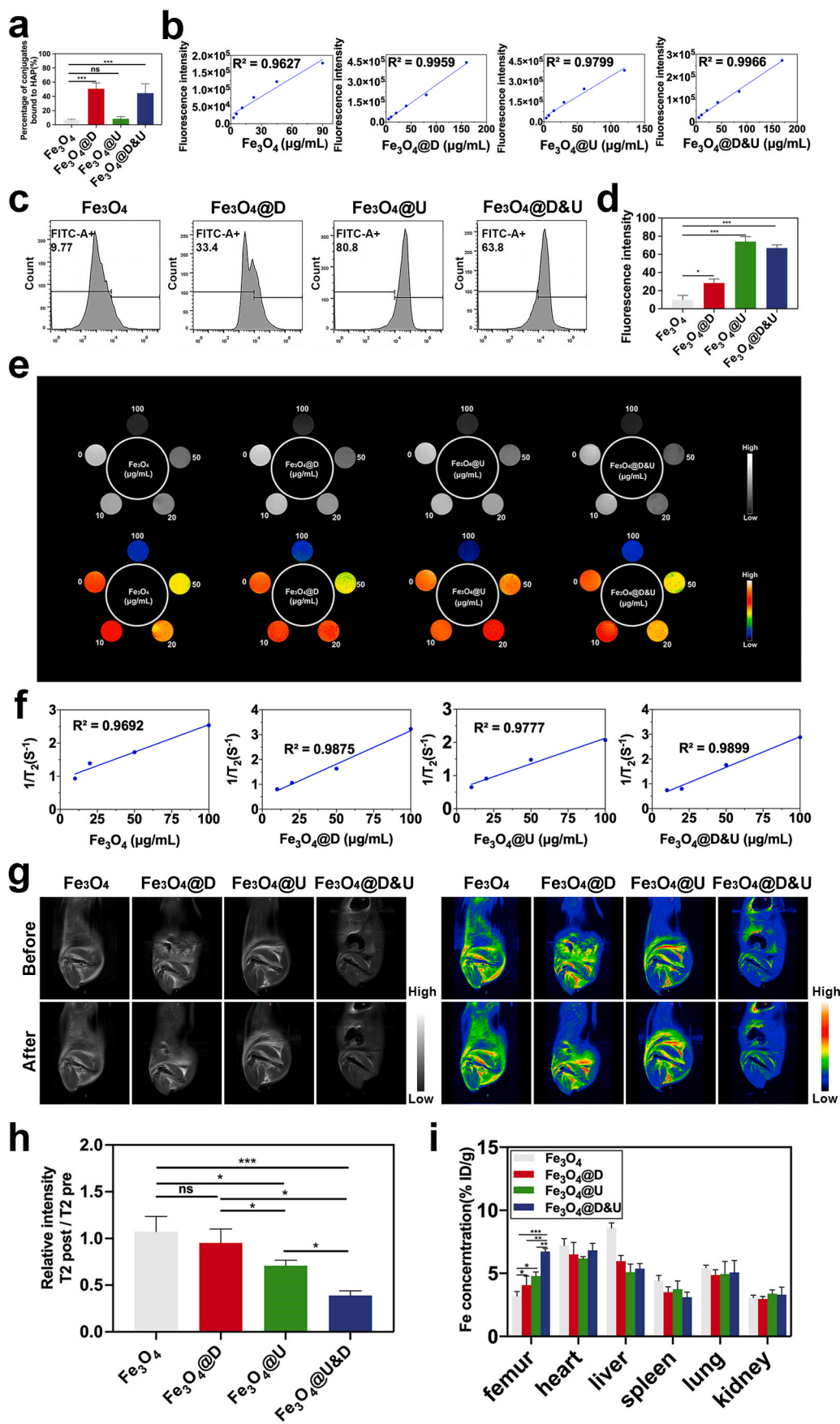
Fig. 1. In vitro and in vivo bone-and-bacteria dual-targeting efficacy of D6 and UBI_{29-41}-modified Fe_3O_4 nanoparticles (NPs). a) In vitro bone targeting efficacy of Fe_3O_4 NPs was characterized with HA binding assay. b) Calibration curve of FITC fluorescence intensity with different concentration of FITC-Fe_3O_4 nanoparticles. c, d) In vitro bacteria targeting efficacy of Fe_3O_4 NPs was characterized with FACS. e) T2-weighted MRI images and their color-coded images of Fe_3O_4 NPs at various concentrations. f) T2 relaxation rates of Fe_3O_4 NPs at different concentrations. g) T2-weighted MRI images and their color-coded images of Fe_3O_4 NPs intravenous administration rats after 30 min. h) Signal intensity of T2* values of the region of interest (ROI) of the infected left femur of rats. i) The amount of Fe in tissues including the femur, heart, liver, spleen, lung, and kidney extracted from the rats. The results are presented as mean ± SD (N = 3). *P < 0.05; **P < 0.01; ***P < 0.001. (For interpretation of the references to color in this figure legend, the reader is referred to the Web version of this article.)
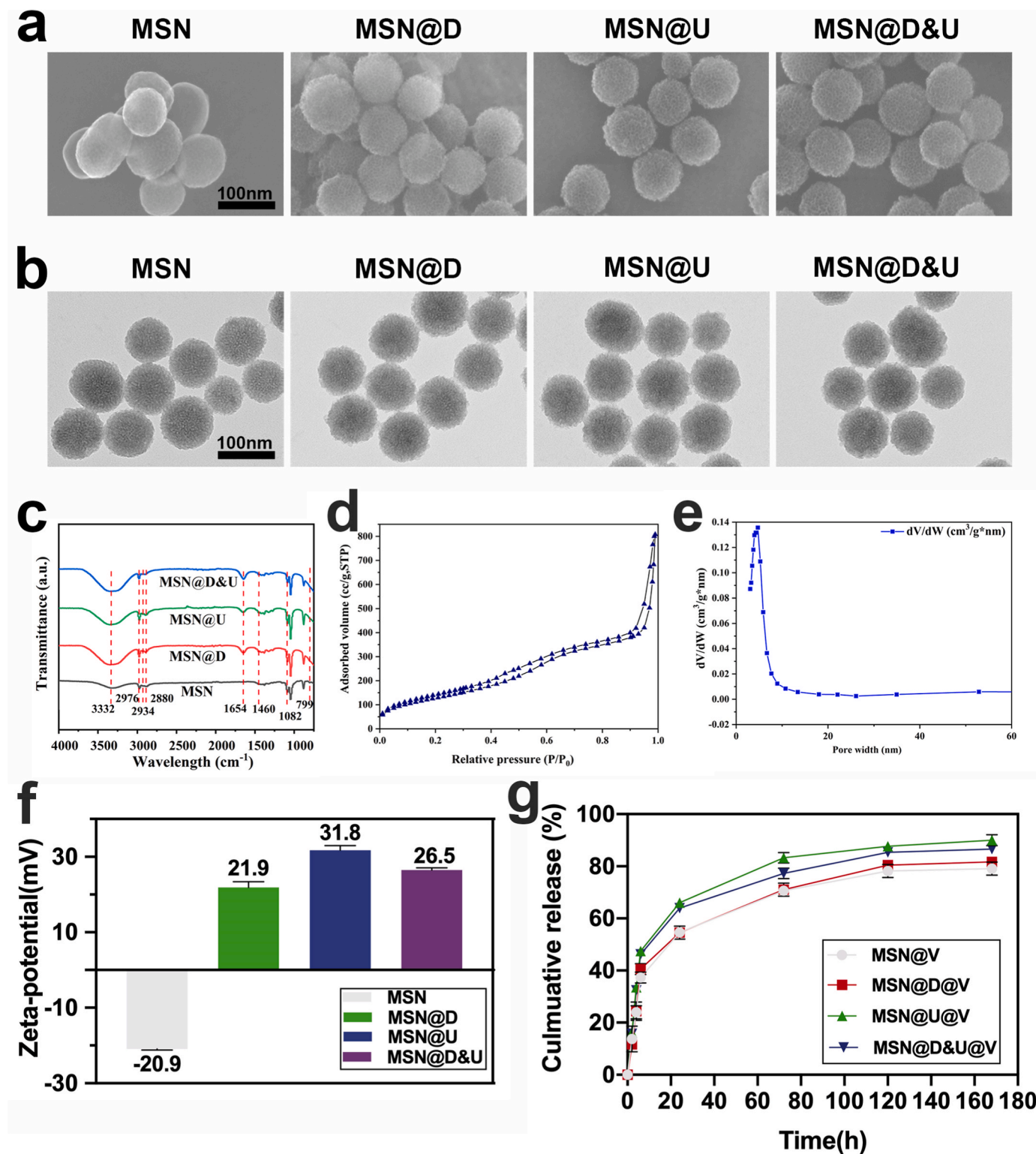
Fig. 2. Characterization of the MSNs. a, b) Characterization of MSNs with Scanning electron microscopy (SEM) and Transmission electron microscopy (TEM), scale bar:100 nm. c) Fourier-transform infrared spectra of MSNs. d, e) N$_2$ adsorption–desorption analysis and pore size distributions of MSN. f) Zeta potential of MSNs. g) Vancomycin release profile of MSNs in vitro.

potential. After the covalent formation of PEG-UBI$_{29-41}$ or PEG-D$_6$/PEG-UBI$_{29-41}$, the zeta potential increased to +31.8 mV and +26.5 mV, respectively. The change in zeta potential proved that MSN had completed amino functionalization, PEGylation, and targeted peptide modification.

3.3. Vancomycin loading and release assays from MSNs

The loading efficiency and release properties of vancomycin were further studied. The vancomycin solution concentrations before and after loading were measured and calculated using an ultraviolet–visible (UV–Vis) spectrophotometer. The maximum UV absorption peak

appeared at 280 nm, indicating the successful loading of vancomycin. The encapsulation efficiency and drug loading efficiency were 19 ± 0.57% and 15.96 ± 0.14%, respectively. The amount of vancomycin released was calculated based on the supernatant vancomycin concentration measured by UV–Vis, and the drug release curves of MSN@V, MSN@D@V, MSN@UBI@V, and MSN@D&U@V are shown in Fig. 2g. After a relatively faster release within 24 h, vancomycin release was sustained. The cumulative release rates of MSN@V, MSN@D@V, MSN@UBI@V, and MSN@D&U@V at 168 h were 81.76%, 82.70%, 90.68%, and 87.60%, respectively. The cumulative release of MSN@UBI@V and MSN@D&U@V at 24 and 168 h was higher compared to the other two groups. This difference may be related to the different zeta potentials of the materials. Those results demonstrated that the synthesized MSNs possessed high dispersity, uniform particle size, high specific surface area, and large pore volume and could sustain release vancomycin for 168 h.

3.4. HA binding capability and bacterial affinity of dual targeting MSNs

To characterize the bone-binding affinity of D6 peptide-modified NPs, the in vitro hydroxyapatite ($Ca_{10}(PO_4)_6(OH)_2$, HA) adsorption assay with FITC-labeled NPs (FITC-NPs) was investigated. HA was selected as a perfect model substrate in that it is a major natural inorganic mineral component of human bones [43]. As shown in Fig. 3a, PEG-D_6 or PEG-D_6 and PEG-UBI_{29-41}-modified NPs (MSN@D, MSN@D&U) exhibited stronger binding with HA in contrast to NPs that were not labeled with peptides D_6 or D_6/UBI_{29-41}. In addition, the FITC fluorescence intensity was identified to be linearly correlated with the concentration of NP (Fig. 3b). The results suggested that PEG-D_6 or PEG-D_6/PEG-UBI_{29-41}-modified MSN had an enhanced bone-targeting capacity. Afterward, we investigated the affinity of MSNs for bacteria in vitro. The bacterial affinity of NPs plays a vital role in antibacterial activity [44].

As shown in Fig. 3c, the interaction of *MRSA* with highly negative unmodified MSNs was low; this is in line with the literature and can be attributed to the strong electrostatic double-layer repulsion between *MRSA* and unmodified MSNs. In contrast, bacterial cells were heavily surrounded by MSN@UBI or MSN@D&U because of the strong specific hydrogen bonding interactions between the well-oriented UBI_{29-41} moieties on the surface of MSN@UBI or MSN@D&U and bacterial cell walls. We further performed flow cytometry experiments to investigate the bacterial affinity of the NPs. Approximately 72.4 ± 2.8% of the FITC-labeled MSN@D&U-treated *MRSA* presented fluorescence (Fig. 3d and e) that was much higher than that of FITC-MSN (2.01 ± 0.35%) and FITC-MSN@D_6 (23.2 ± 2.8%) treated *MRSA* cells. Thus, the flow cytometry results demonstrated that PEG-UBI_{29-41}- or PEG-D_6/UBI_{29-41}-modified NPs showed enhanced bacterial affinity. In the present study, D_6-modified NPs greatly improved the bone-targeting performance. Our results also demonstrated that UBI_{29-41}-modified NPs possessed increased bacterial affinity, which could enhance thetherapeutic effect.

3.5. The antibacterial activity of the NPs against MRSA

Traditional antibiotic treatment poses an enormous risk by causing antibiotic resistance and serious adverse reactions in the post-antibiotic era [45], which may lead to more severe toxic symptoms [46,47]. To cope with this challenge, targeted delivery strategies based on NPs have recently been applied to treat infections with relatively low antibiotic doses and decreased adverse effects [48]. In this study, we successfully constructed a vancomycin-loaded NP with bone-and-bacteria dual-targeting properties to target bacterial infected bone sites. To determine the antibacterial activity of the NPs against *MRSA*, we conducted minimum inhibitory concentration (MIC) experiments. MSN@UBI@V and MSN@D&U@V had the strongest inhibitory effects on the growth of *MRSA* cells. The MIC values of MSN@V, MSN@D@V MSN@UBI@V, and MSN@D&U@V against *MRSA* were 32, 32, 16, and 16 µg mL^{-1}

(Table S1), respectively. Compared to MSN@V and MSN@D@V, MSN@UBI@V and MSN@D&U@V exhibited stronger antibacterial effects. One of the reasons may be that MSN@UBI@V and MSN@D&U@V released more vancomycin within 24 h. Another emerging reason for this divergence in results is the presence of UBI_{29-41}, a cationic human antimicrobial peptide, which showed high sensitivity, specificity, and accuracy in detecting bacterial infection [29,49]. For these reasons, MSN@UBI@V and MSN@D&U@V exhibited superior antibacterial effects on MSN@V and MSN@D@V in vitro.

Morphological changes in *MRSA* were characterized by SEM to estimate the antibacterial activity of MSNs@V. The untreated bacteria had normal shapes, clear borders, and membrane integrity, whereas MSNs@V-treated bacterial membranes were seriously damaged and highly distorted from the original morphology (Fig. 4a). Many of the NPs accumulated on the surface of the cells, especially in the MSN@UBI@V and MSN@D&U@V groups, which is consistent with the results shown in Fig. 3c.

Biofilms are widely recognized to act as a crucial role in the pathogenesis of bacterial infections [50]. However, owing to the difficulty for antibiotics to penetrate the biofilm matrix, biofilms are the main cause of therapy failure and recurring infections. Therefore, it is important to impair or inhibit biofilm formation during treatment. We investigated the biofilm inhibition effect on the Ti surface of MSNs@V by confocal laser scanning microscopy (CLSM) (Fig. 4b). Encouragingly, after MSNs@V or vancomycin therapy, bacteria colonized the Ti disc exhibited a lesser amount than bacteria in the MSN group. In addition, the bacterial biofilms were stained with 1% crystal violet and quantified using optical density measurements after incubation at 37 °C for 24 h (Fig. 4c and d). The results indicated that MSNs@V, especially MSN@UBI@V and MSN@D&U@V groups, significantly decreased bacterial adherence to Ti. We further evaluated the killing kinetics of MSNs@V. The optical density (OD) values of *MRSA* suspensions incubated with MSNs@V at their respective MICs for 12 h were continuously recorded to quantify bacterial growth. The bacteria grew rapidly within 12 h, after which the growth entered the stationary phase. As depicted in Fig. 4e, bacterial growth was completely inhibited by the four MSNs@V. These results indicate that MSNs@V strongly inhibited bacterial growth.

Biofilms from different groups were further observed using SEM. However, many bacterial colonies formed a dense shield on the Ti discs in the control group. In contrast, all treatment groups showed a reduction in bacterial colonies. When the SEM micrographs were captured at high magnification, the impaired cell membranes of bacteria treated with MSNs@V were clearly observed (Fig. 4f). In summary, our results demonstrated that MSNs@V, especially MSN@UBI@V and MSN@D&U@V, possessed excellent antibacterial activity and could be used to eradicate *MRSA*-related infections in vitro.

3.6. Biocompatibility of MSNs

As biosafety assessment is necessary for potential clinical applications, cytotoxicity tests were carried out to evaluate the safety of the MSNs [51]. The MSNs were co-cultured with rat bone marrow mesenchymal stem cells (rBMSCs) for 1, 3, and 5 d at various concentrations (for MSNs: from 0 to 500 µg mL^{-1}), and the cytotoxicity of the particles was evaluated by cell counting kit-8 (CCK-8) assay (Fig. 5a). The results revealed that the cell viability of rBMSCs remained above 90% when the MSN concentration range was 0–100 µg mL^{-1}, and the cell viability was approximately 80% when the concentration range was 100–200 µg mL^{-1}. However, when the concentration was 500 µg mL^{-1}, the cell viability was less than 30%. Compared to the control group, i.e., MSNs, MSN@D, MSN@UBI, and MSN@D&U showed relatively high cell viability. When the concentration range was 0–200 µg mL^{-1}, cell viability was maintained above 90%. As time increased from 1 to 5 d, the cell viability of rBMSCs cocultured with MSN@D, MSN@UBI, and MSN@D&U decreased slightly but was still higher than 80% at a concentration of 500 µg mL^{-1}, which indicated that the MSNs had good cell
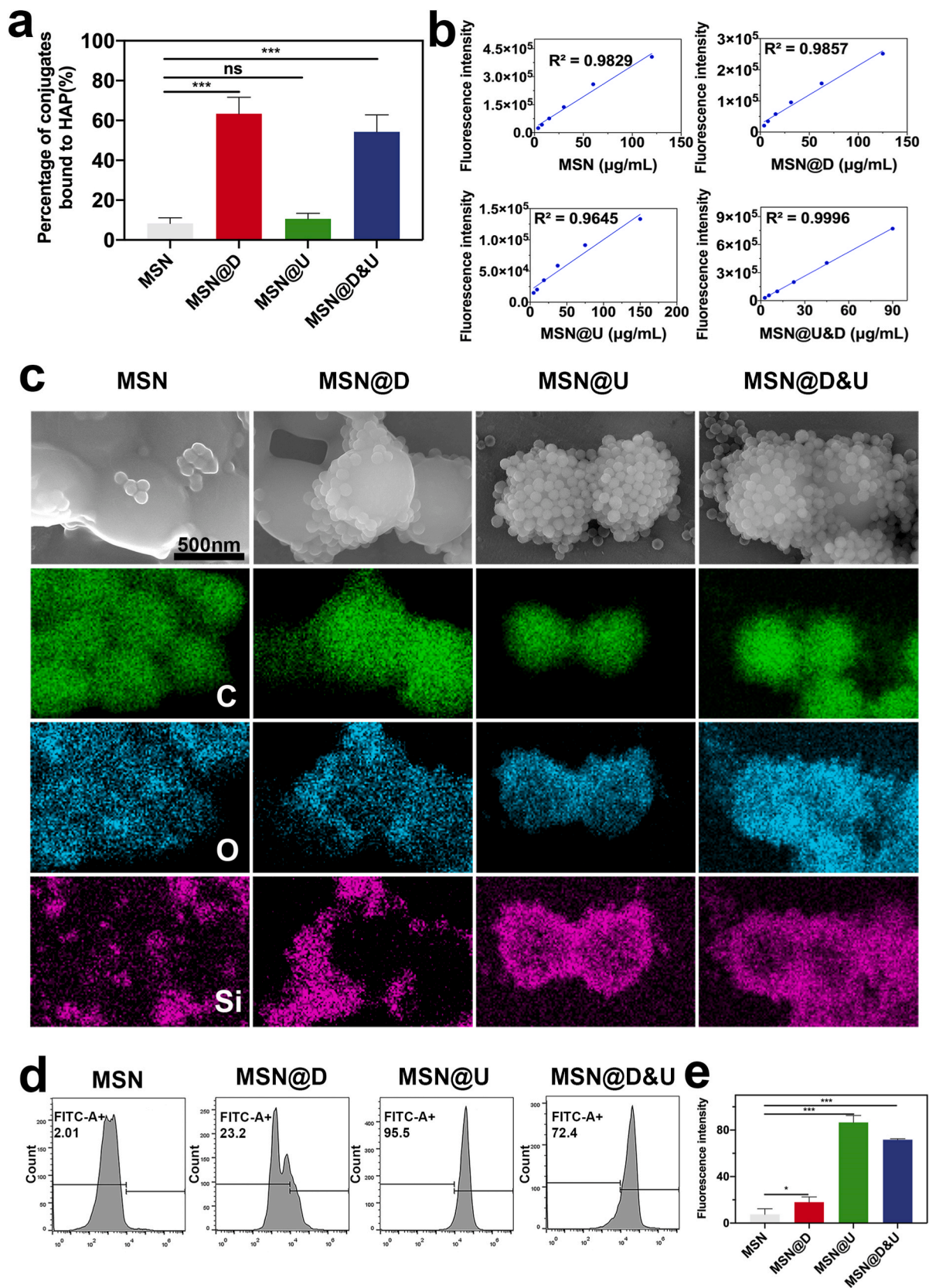
Fig. 3. In vitro bone and bacteria targeting of MSNs. a) MSNs binding to HA was detected at 4 h. b) Calibration curve of FITC fluorescence intensity with different concentration of FITC-NPs. c) SEM and elemental mapping image of *MRSA* after treating with MSNs, scale bar:500 nm. d) Binding the FITC-labeled MSNs to *MRSA*, as measured by FACS. e) Quantitative analysis of the binding efficacy of the FITC-labeled MSNs to *MRSA*, as measured by FACS. The results are presented as mean ± SD (N = 3). *P < 0.05; **P < 0.01; ***P < 0.001.
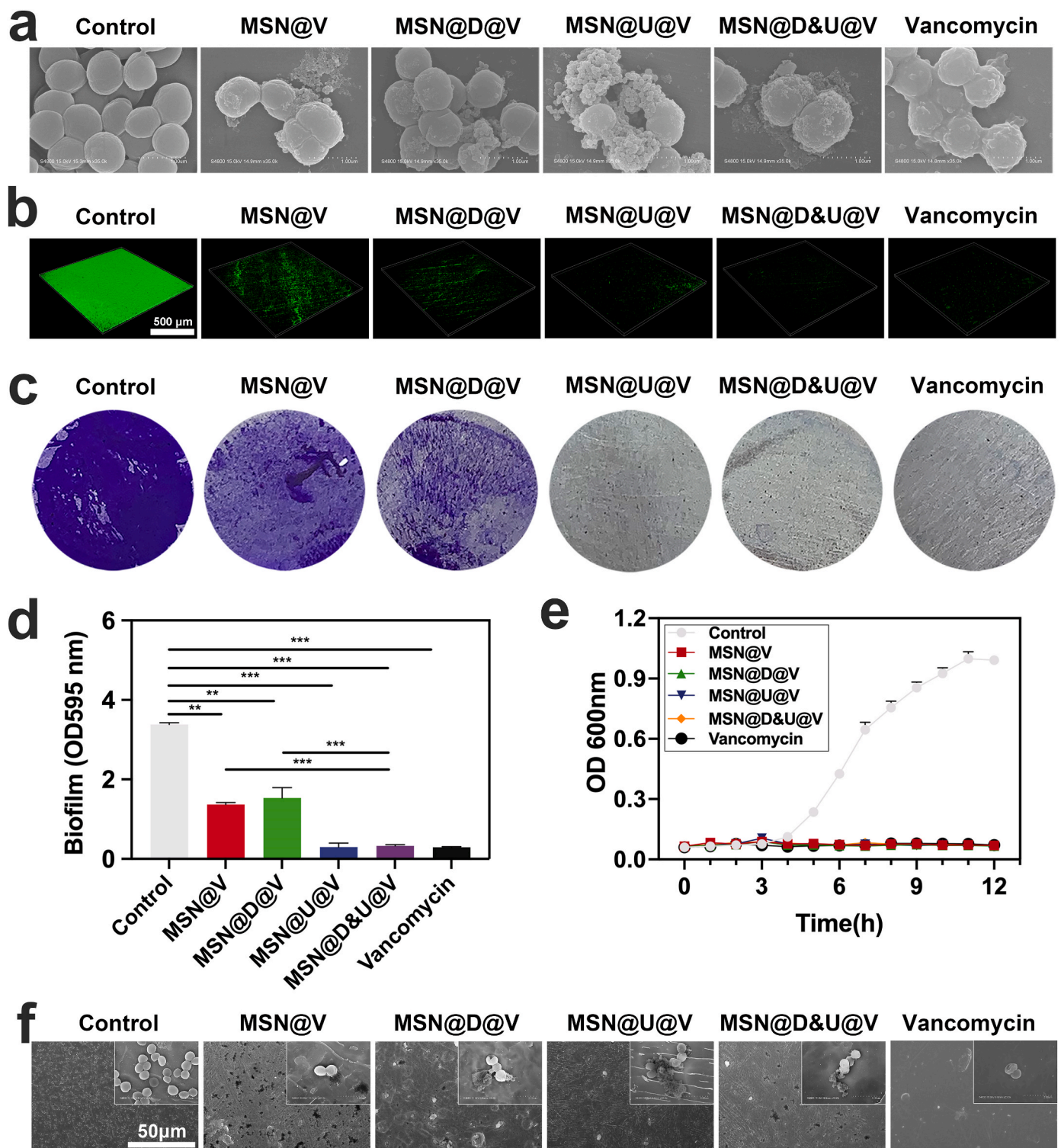
Fig. 4. Antimicrobial efficacy of MSNs and vancomycin in vitro. a) SEM images of *MRSA* with MSNs or vancomycin for 6 h, scale bar: 1 μm. b) confocal laser scanning microscopy (CLSM) images of biofilms treated with MSNs or vancomycin at respective MICs for 24 h and stained with a bacteria live-dead kit, scale bar: 500 μm (Green represents live bacteria and the red represent dead bacteria). c) Biofilms treated with MSNs or vancomycin at respective MICs for 24 h and stained with 1% crystal violet. d) Quantify biofilm formation by using a microtiter plate reader. e) Time-dependent killing of *MRSA* by MSNs and vancomycin at the concentration of minimum inhibitory concentration (MIC). f) SEM images of biofilms treated with MSNs or vancomycin at respective MICs for 24 h, scale bar: 50 μm. Results are presented as mean ± SD (N = 3). *P < 0.05; **P < 0.01; ***P < 0.001. (For interpretation of the references to color in this figure legend, the reader is referred to the Web version of this article.)
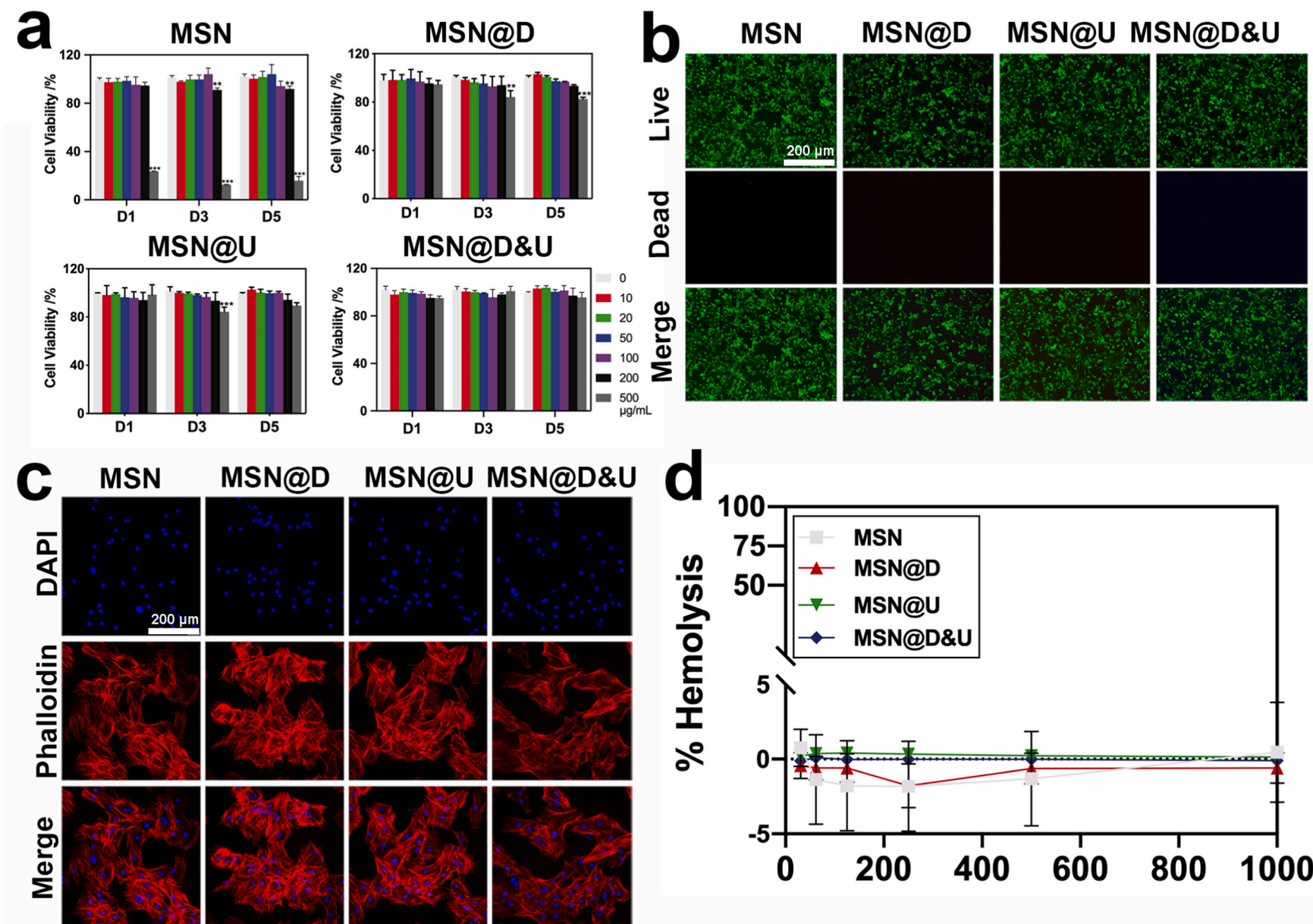
Fig. 5. Biocompatibility and hemolytic activity of MSNs in vitro. a) Cell viability of rat bone marrow mesenchymal stem cells (rBMSCs) after treatment with the MSNs at different concentrations after 1, 3, and 5 d. b) Fluorescence microscopy images of rBMSCs were investigated after a 24 h treatment with MSNs, scale bar: 200 μm. c) CLSM analysis of the morphology of rBMSCs after 24 h treatment with MSNs, scale bar: 200 μm. d) The hemolytic activity of MSNs. The results are presented as mean ± SD (N = 3). *P < 0.05; **P < 0.01; ***P < 0.001; ****P < 0.0001.

compatibility and low toxicity. Live/dead staining and cell morphology assays were further applied to characterize the effect of NPs on cell viability. rBMSCs exhibited normal shapes after incubation for 24 h with NPs at a concentration of 64 μg mL^{-1}. This indicated that MSNs did not cause any cell deformities or inactivation (Fig. 5b and c). These results suggest that the NPs synthesized in this study had no apparent toxicity to rBMSCs. Hemolytic activity assays are critical for evaluating the hemocompatibility of NPs under physiological conditions [52]. Fig. 5d shows the curve of the hemolysis rate versus particle concentration (0–1000 μg mL^{-1}). Notably, none of the synthetic MSNs tested showed hemolytic activity at the investigated concentrations. Overall, our results demonstrated that the NPs used in this study were nontoxic within a certain range.

3.7. In vivo therapy of orthopedic implant-related infection and histochemistry analysis

Encouraged by the outstanding infection eradication ability in vitro, we further validated the anti-infective effect using a rat model of orthopedic implant-related infection with *MRSA*. Rats were treated with phosphate buffered saline (PBS), MSN@V, MSN@D@V, MSN@UBI@V, MSN@D&U@V, and vancomycin via daily tail vein injections for 3 weeks. Bone destruction around the implant was observed by X-ray examination 3 weeks after surgery, and skeletal muscle tissues were harvested and fixed, as shown in Fig. 6a. The rats in the control group presented obvious radiographic characteristic signs of bone implant-related infection, as demonstrated by the osteolysis and periosteal reactions around the implant [53]. The destruction of the femur was relieved after treatment with MSN@V, MSN@D@V, MSN@UBI@V, MSN@D&U@V, and vancomycin. Among all the treatment groups, MSN@D&U@V exhibited the greatest reduction in bone destruction and maintained bone integrity, superior to the MSN@V, MSN@D@V, MSN@UBI@V, and vancomycin groups. A quantitative result of the X-ray photographs was shown in Fig. 6b. The radiographic scores after treatment with PBS, MSN@V, MSN@D@V, MSN@UBI@V, MSN@D&U@V, and vancomycin were 7.77 ± 0.63, 5.2 ± 0.2, 4.7 ± 0.2, 3.8 ± 0.3, 2.17 ± 0.17, and 3.83 ± 0.19, respectively. The MSN@D&U@V group had significantly lower mean scores than the other groups ($P < 0.05$). As shown in Fig. 6c, the trend of the inflammatory reaction in the articular cavity was the same as the imaged features, and rats in the control group exhibited typical clinical symptoms of orthopedic implant-related infection, including intramedullary pus formation, periosteal reactions, osteolytic lesions, and bone deformities. However, treatment appeared to reduce the severity of these symptoms, and MSN@D&U@V was free from infection. The mean pathology scores of bone gross after treatment with PBS, MSN@V, MSN@D@V, MSN@UBI@V, MSN@D&U@V, and vancomycin were 3.64 ± 0.31, 3.1 ± 0.18, 2.98 ± 0.22, 2.45 ± 0.19, 1.89 ± 0.17, and 2.53 ± 0.21, respectively (Fig. 6d). The mean score of MSN@D&U@V significantly decreased ($P < 0.05$) compared to the other groups. Microcomputed tomography (micro-CT) was used to analyze the bone tissue around the Ti implant. As shown in Fig. 6e, no significant signs of orthopedic implant-related infection were observed in the MSN@D&U@V group. In the MSN@D&U@V group, the values of bone volume per tissue volume (BV/TV) and trabecular thickness (Tb. Th) were higher, whereas the trabecular separation (Tb. Sp) value for implants was lower compared to other groups (Fig. 6f), suggesting that bone destruction was least severe, which is consistent with the results determined by X-rays.

The left femurs of sacrificed rats were harvested for bacterial load derivation from the homogenates of the bone tissues. As shown in Figs. S10a and S10b, the number of colonies on the bone around the Ti implant after treatment with MSN@D&U@V was lowest within a given treatment group. Meanwhile, Ti implants were dissected, and surface bacteria were detached by sonication. The number of bacteria on the Ti implant in the MSN@D&U@V group was also the lowest among all

groups (Figs. S10c and S10d). These results confirmed that the MSN@D&U@V group had significantly fewer bacteria in the bone tissue around the Ti implants than all the other groups. To visualize the attached bacteria on the Ti rod, we performed live/dead bacteria staining by CLSM (Leica TCS SP2, Heidelberg, Germany). The results showed that the number of viable bacteria in the MSN@D&U@V group was lowest among all the treated groups (Fig. 6g). Moreover, the SEM measurements of the extracted Ti rods showed consistent results (Fig. 6h).

Furthermore, the inflammatory reaction of the decalcified bone tissue was evaluated by hematoxylin and eosin (H&E) staining, and the bacterial residue in peri-implant bone tissues was detected by Gram staining. As shown in Fig. 6i, the canonical signs of inflammatory responses were noted in the untreated groups, which presented significant inflammatory exudation and a large number of lymphocytes, monocytes, and neutrophil infiltration in H&E staining. Meanwhile, a large number of bacteria were observed by Gram staining in the control group (Fig. 6j). In contrast, both inflammatory cells and bacteria were significantly reduced in the MSN@D&U@V group, which was consistent with the results of the microbiological analysis. Therefore, the results of histological evaluation demonstrated that MSN@D&U@V possessed excellent antibacterial ability in vivo. Finally, the organs (heart, spleen, liver, lung, and kidney) of rats were obtained for physiopathological studies to evaluate the adverse effects of MSN@D&U@V.

As depicted in Fig. 7, there were no obvious abnormalities or damages in the main organs of the rats, indicating that the dual-targeting drug delivery vehicle was biologically safe.

4. Conclusions

Bone-and-bacteria dual-targeted Fe$_3$O$_4$ NPs could be achieved by covalent peptide PEG-D$_6$ and PEG-UBI$_{29-41}$ molecules on the Fe$_3$O$_4$ NP surface, and the dual-targeted NPs could precisely target the bone infection site. This indicated that PEG-D$_6$ and PEG-UBI$_{29-41}$ could be excellent targets for delivering NPs to the bone infection site. It was further proved that the dual-targeted Fe$_3$O$_4$@D&U nanocomposites exerted an excellent ability for early diagnosis of orthopedic implant related infection by specific targeting to the infected tissue and significantly decreased T2 SI of the bacteria-infected femur of rats. The PEG-D$_6$- and PEG-UBI$_{29-41}$-modified MSN nanocomposites also exhibited excellent bone-targeting and bacteria-targeting functions. The results of ex vivo assay indicated that dual-targeted MSN@D&U@V nanocomposites possessed excellent antibacterial activity and could be used to eradicate *MRSA*-related infections. Owing to its superior antibacterial activity, MSN@D&U@V proved to be more efficient in treating orthopedic implant related infection than vancomycin. Moreover, MSN@D&U@V nano composite demonstrated good biocompatibility. In summary, our results demonstrated that PEG-D$_6$- and PEG-UBI$_{29-41}$-modified NPs exhibited excellent targeting to bone infection sites and could control the release of vancomycin at the bone infection site to enhance the treatment of orthopedic implant-related infection.

Declaration of competing interest

The authors declare no competing interests.

CRediT authorship contribution statement

Bin'en Nie: Conceptualization, Methodology, Investigation, Writing – original draft, Data curation. **Shicheng Huo:** Conceptualization, Methodology, Validation, Investigation. **Xinhua Qu:** Conceptualization, Methodology, Investigation, Data curation. **Jingjing Guo:** Investigation, Data curation, Methodology. **Xi Liu:** Methodology. **Qimin Hong:** Methodology, Investigation. **You Wang:** Conceptualization, Resources. **Jianping Yang:** Conceptualization, Methodology, Investigation. **Bing Yue:** Conceptualization, Resources, Supervision, Project administration,
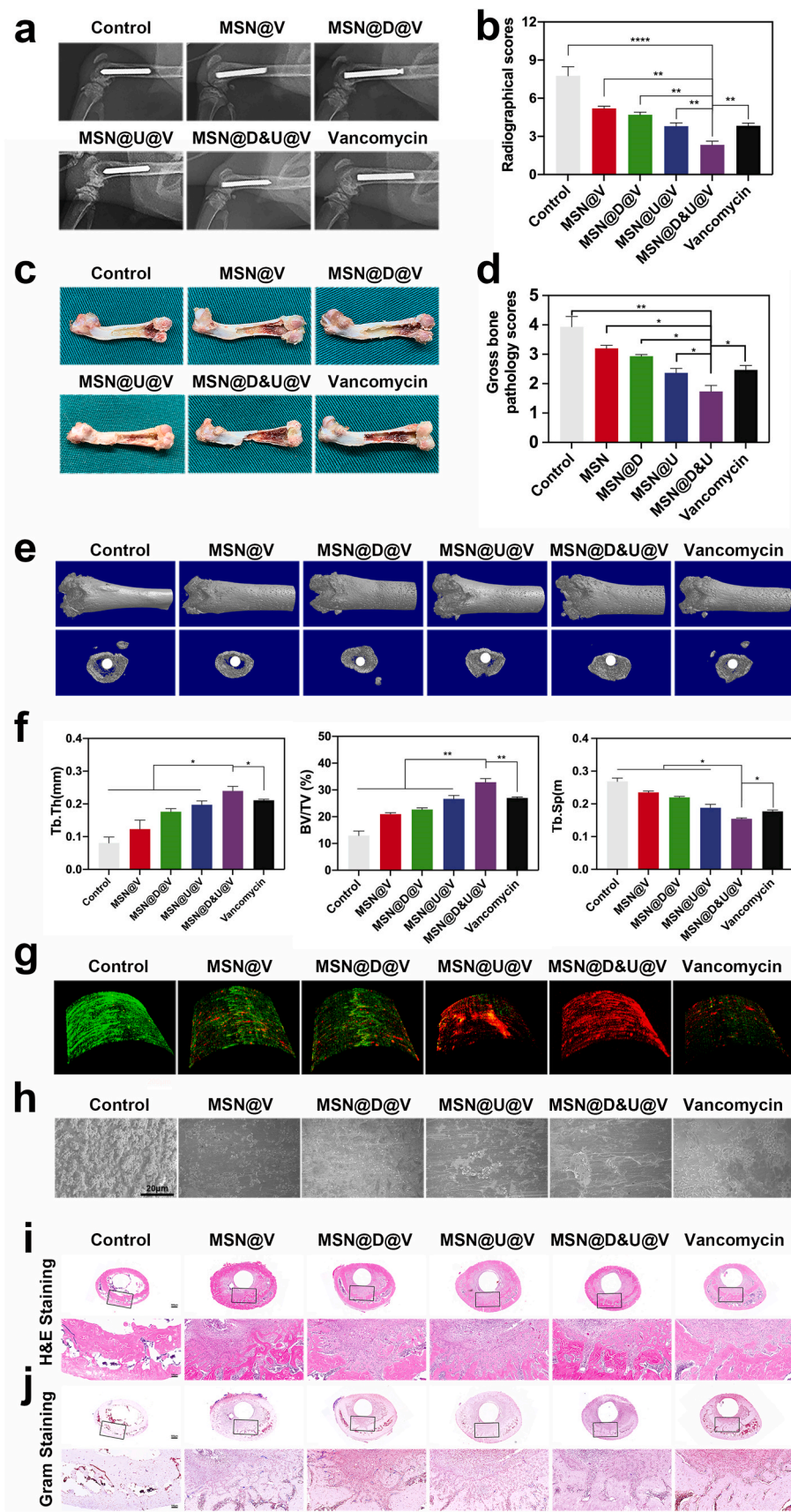
Fig. 6. Systematic evaluation of the antibacterial effect of MSN@V NPs in vivo using the rat implant-related *MRSA*-infection model. a) After 3 weeks of the titanium implantation, X-ray image was used to analysis the osteolysis that result from implant-related infection. b) Radiographic scores. c) After 3 weeks of titanium implantation, gross images of the titanium implant around the bone tissue were analyzed. d) Gross bone pathology scores of the femur. e) Microcomputed tomography (micro-CT) images of samples implanted for 3 weeks. f) Quantitative analysis results from micro-CT evaluation. g, h) CLSM and SEM images of extracted implants to characterize bacteria viability, scale bar: 400 μm and 20 μm respectively. (Green represents live bacteria and the red represent dead bacteria). i, j) Hematoxylin and eosin and Gram staining of decalcified bone slices obtained after 3 weeks, scale bar: 1000 μm and 200 μm respectively. The results are presented as mean ± SD (N = 3). *$P < 0.05$; **$P < 0.01$; ***$P < 0.001$. (For interpretation of the references to color in this figure legend, the reader is referred to the Web version of this article.)
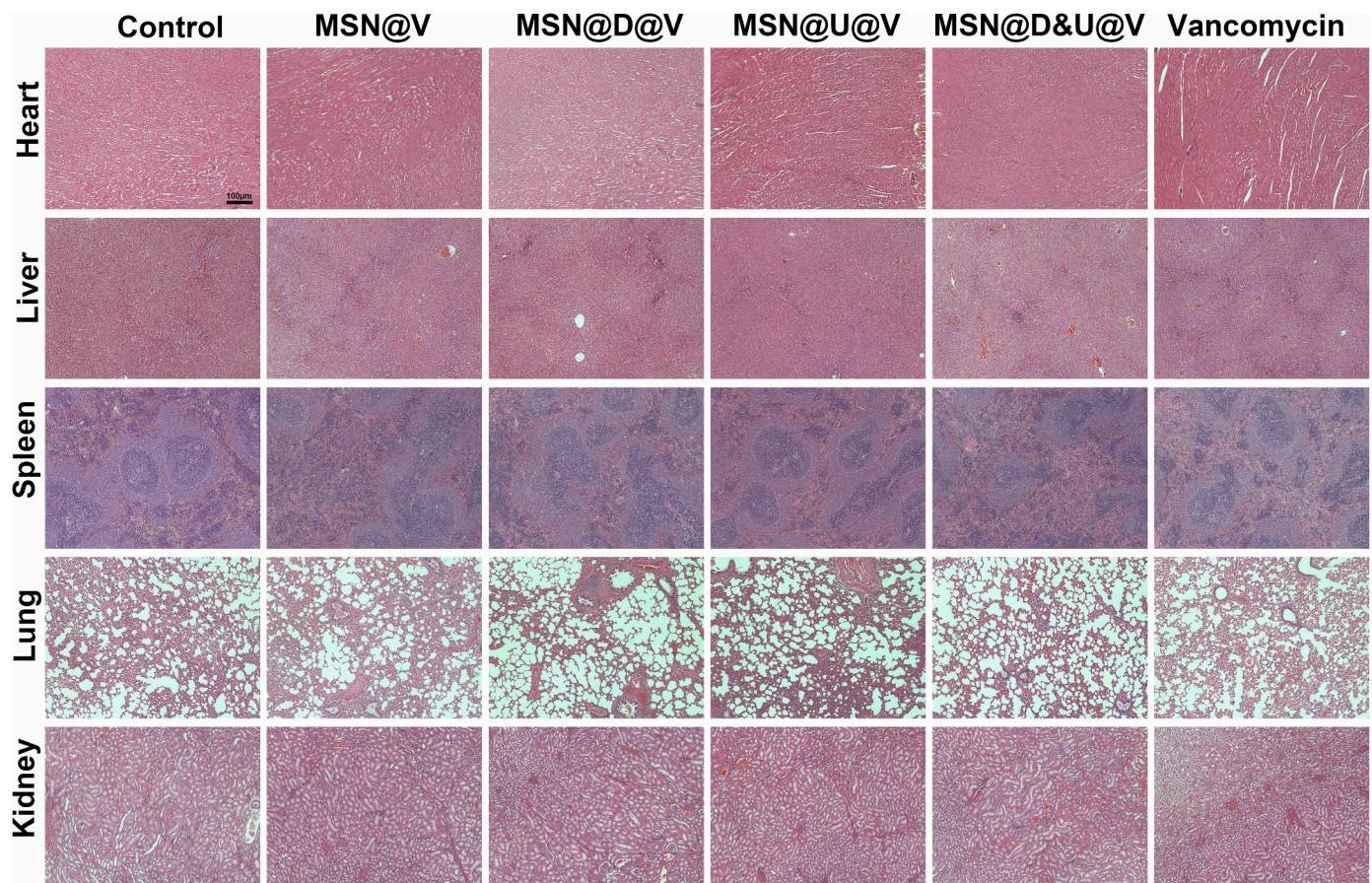
Fig. 7. Histological evaluation of heart, liver, spleen, lung, and kidney after treatment with MSNs. Scale bar: 100 μm.

Funding acquisition, Writing – review & editing.

Appendix A. Supplementary data

Supplementary data to this article can be found online at https://doi.org/10.1016/j.bioactmat.2022.02.003.

References

[1] K.T. Peng, Y.C. Chiang, T.Y. Huang, P.C. Chen, P.J. Chang, C.W. Lee, Curcumin nanoparticles are a promising anti-bacterial and anti-inflammatory agent for treating periprosthetic joint infections, Int. J. Nanomed. 14 (2019) 469–481.

[2] X. Yuan, L. Ouyang, Y. Luo, Z. Sun, C. Yang, J. Wang, X. Liu, X. Zhang, Multifunctional sulfonated polyetheretherketone coating with beta-defensin-14 for yielding durable and broad-spectrum antibacterial activity and osseointegration, Acta Biomater. 86 (2019) 323–337.

[3] A. Premkumar, D.A. Kolin, K.X. Farley, J.M. Wilson, A.S. McLawhorn, M.B. Cross, P.K. Sculco, Projected economic burden of periprosthetic joint infection of the hip and knee in the United States, J. Arthroplasty 36 (5) (2021) 1484–1489, e3.

[4] K. Kusejko, Á. Aunón, B. Jost, B. Natividad, C. Strahm, C. Thurnheer, D. Pablo-Marcos, D. Slama, G. Scanferla, I. Uckay, I. Waldmann, J. Esteban, J. Lora-Tamayo, M. Clauss, M. Fernandez-Sampedro, M. Wouthuyzen-Bakker, M.C. Ferrari, N. Gassmann, P. Sendi, P. Jent, P.C. Morand, P. Vijayvargiya, R. Trebše, R. Patel, R. D. Kouyos, S. Corvec, T.S. Kramer, V.A. Stadelmann, Y. Achermann, The impact of surgical strategy and rifampin on treatment outcome in cutibacterium periprosthetic joint infections, Clin. Infect. Dis. 72 (12) (2021) e1064–e1073.

[5] N.J. Hickok, I.M. Shapiro, Immobilized antibiotics to prevent orthopaedic implant infections, Adv. Drug Deliv. Rev. 64 (12) (2012) 1165–1176.

[6] M.E. Neufeld, B.A. Lanting, M. Shehata, J.L. Howard, S.J. MacDonald, M.G. Teeter, E.M. Vasarhelyi, Prevalence and outcomes of unexpected positive intraoperative cultures in presumed aseptic revision hip arthroplasty, J Bone Joint Surg Am 103 (15) (2021) 1392–1401.

[7] T. Falstie-Jensen, J. Lange, H. Daugaard, M.H. Vendelbo, A.K. Sørensen, B. Zerahn, J. Ovesen, K. Søballe, L.C. Gormsen, 18F FDG-PET/CT has poor diagnostic accuracy in diagnosing shoulder PJI, Eur. J. Nucl. Med. Mol. Imag. 46 (10) (2019) 2013–2022.

[8] P. Bémer, J. Léger, S. Milin, C. Plouzeau, A.S. Valentin, N. Stock, A. Jolivet-Gougeon, A. Moreau, S. Corvec, I. Quintin-Roue, D. Tandé, G. Héry-Arnaud, M. C. Rousselet, C. Lemarié, M. Kempf, P. Michenet, L. Bret, G. de Pinieux, C. Burucoa, Histopathological diagnosis of prosthetic joint infection: does a threshold of 23 neutrophils do better than classification of the periprosthetic membrane in a prospective multicenter study? J. Clin. Microbiol. 56 (9) (2018).

[9] W. Zimmerli, A. Trampuz, P.E. Ochsner, Prosthetic-joint infections, N. Engl. J. Med. 351 (16) (2004) 1645–1654.

[10] E. Tshibangu-Kabamba, Y. Yamaoka, Helicobacter pylori infection and antibiotic resistance - from biology to clinical implications, Nat. Rev. Gastroenterol. Hepatol. 18 (9) (2021) 613–629.

[11] E. Rossi, R. La Rosa, J.A. Bartell, R.L. Marvig, J.A.J. Haagensen, L.M. Sommer, S. Molin, H.K. Johansen, Pseudomonas aeruginosa adaptation and evolution in patients with cystic fibrosis, Nat. Rev. Microbiol. 19 (5) (2021) 331–342.

[12] T. Diallo, M. Adjobimey, R. Ruslami, A. Trajman, O. Sow, J. Obeng Baah, G. B. Marks, R. Long, K. Elwood, D. Zielinski, M. Gninafon, D.A. Wulandari, L. Apriani, C. Valiquette, F. Fregonese, K. Hornby, P.Z. Li, P.C. Hill, K. Schwartzman, A. Benedetti, D. Menzies, Safety and side effects of rifampin versus isoniazid in children, N. Engl. J. Med. 379 (5) (2018) 454–463.

[13] Y. Wang, X. Ding, Y. Chen, M. Guo, Y. Zhang, X. Guo, H. Gu, Antibiotic-loaded, silver core-embedded mesoporous silica nanovehicles as a synergistic antibacterial agent for the treatment of drug-resistant infections, Biomaterials 101 (2016) 207–216.

[14] S. Zhang, X. Qu, J. Jiao, H. Tang, M. Wang, Y. Wang, H. Yang, W. Yuan, B. Yue, Felodipine enhances aminoglycosides efficacy against implant infections caused by methicillin-resistant Staphylococcus aureus, persisters and biofilms, Bioact Mater. (2021), https://doi.org/10.1016/j.bioactmat.2021.11.019.

[15] Y. Wang, W. Teng, Z. Zhang, X. Zhou, Y. Ye, P. Lin, A. Liu, Y. Wu, B. Li, C. Zhang, X. Yang, W. Li, X. Yu, Z. Gou, Z. Ye, A trilogy antimicrobial strategy for multiple infections of orthopedic implants throughout their life cycle, Bioact Mater. 6 (7) (2021) 1853–1866.

[16] W. Guan, L. Tan, X. Liu, Z. Cui, Y. Zheng, K.W.K. Yeung, D. Zheng, Y. Liang, Z. Li, S. Zhu, X. Wang, S. Wu, Ultrasonic interfacial engineering of red phosphorous-metal for eradicating MRSA infection effectively, Adv. Mater. 33 (5) (2021), e2006047.

[17] B. Huang, L. Tan, X. Liu, J. Li, S. Wu, A facile fabrication of novel stuff with antibacterial property and osteogenic promotion utilizing red phosphorus and near-infrared light, Bioact Mater. 4 (1) (2019) 17–21.

[18] M. Li, L. Li, K. Su, X. Liu, T. Zhang, Y. Liang, D. Jing, X. Yang, D. Zheng, Z. Cui, Z. Li, S. Zhu, K.W.K. Yeung, Y. Zheng, X. Wang, S. Wu, Highly effective and noninvasive near-infrared eradication of a Staphylococcus aureus biofilm on implants by a photoresponsive coating within 20 min, Adv. Sci. 6 (17) (2019) 1900599.

[19] K. Su, L. Tan, X. Liu, Z. Cui, Y. Zheng, B. Li, Y. Han, Z. Li, S. Zhu, Y. Liang, X. Feng, X. Wang, S. Wu, Rapid photo-sonotherapy for clinical treatment of bacterial infected bone implants by creating oxygen deficiency using sulfur doping, ACS Nano 14 (2) (2020) 2077–2089.

[20] L. Tan, J. Li, X. Liu, Z. Cui, X. Yang, S. Zhu, Z. Li, X. Yuan, Y. Zheng, K.W.K. Yeung, H. Pan, X. Wang, S. Wu, Rapid biofilm eradication on bone implants using red phosphorus and near-infrared light, Adv. Mater. 30 (31) (2018), e1801808.

[21] Y. Wang, Y. Yang, Y. Shi, H. Song, C. Yu, Antibiotic-free antibacterial strategies enabled by nanomaterials: progress and perspectives, Adv. Mater. 32 (18) (2020), e1904106.

[22] S. Yang, X. Han, Y. Yang, H. Qiao, Z. Yu, Y. Liu, J. Wang, T. Tang, Bacteria-targeting nanoparticles with microenvironment-responsive antibiotic release to eliminate intracellular Staphylococcus aureus and associated infection, ACS Appl. Mater. Interfaces 10 (17) (2018) 14299–14311.

[23] S. Hussain, J. Joo, J. Kang, B. Kim, G.B. Braun, Z.G. She, D. Kim, A.P. Mann, T. Mölder, T. Teesalu, S. Carnazza, S. Guglielmino, M.J. Sailor, E. Ruoslahti, Antibiotic-loaded nanoparticles targeted to the site of infection enhance antibacterial efficacy, Nat. Biomed. Eng. 2 (2) (2018) 95–103.

[24] S.G. Rotman, T.F. Moriarty, B. Nottelet, D.W. Grijpma, D. Eglin, O. Guillaume, Poly (Aspartic acid) functionalized poly(ε-caprolactone) microspheres with enhanced hydroxyapatite affinity as bone targeting antibiotic carriers, Pharmaceutics 12 (9) (2020) 885.

[25] S. Kasugai, R. Fujisawa, Y. Waki, K. Miyamoto, K. Ohya, Selective drug delivery system to bone: small peptide (Asp)6 conjugation, J. Bone Miner. Res. 15 (5) (2000) 936–943.

[26] X. Gao, L. Li, X. Cai, Q. Huang, J. Xiao, Y. Cheng, Targeting nanoparticles for diagnosis and therapy of bone tumors: opportunities and challenges, Biomaterials 265 (2021) 120404.

[27] Y. Liu, P. Yu, X. Peng, Q. Huang, M. Ding, Y. Chen, R. Jin, J. Xie, C. Zhao, J. Li, Hexapeptide-conjugated calcitonin for targeted therapy of osteoporosis, J. Contr. Release 304 (2019) 39–50.

[28] T. Takahashi, K. Yokogawa, N. Sakura, M. Nomura, S. Kobayashi, K. Miyamoto, Bone-targeting of quinolones conjugated with an acidic oligopeptide, Pharm. Res. (N. Y.) 25 (12) (2008) 2881–2888.

[29] H. Chen, C. Liu, D. Chen, K. Madrid, S. Peng, X. Dong, M. Zhang, Y. Gu, Bacteria-targeting conjugates based on antimicrobial peptide for bacteria diagnosis and therapy, Mol. Pharm. 12 (7) (2015) 2505–2516.

[30] M. Assadi, K. Vahdat, I. Nabipour, M.R. Sehhat, F. Hadavand, H. Javadi, A. Tavakoli, J. Saberifard, M.R. Kalantarhormozi, A. Zakani, M. Eftekhari, Diagnostic value of 99mTc-ubiquicidin scintigraphy for osteomyelitis and comparisons with 99mTc-methylene diphosphonate scintigraphy and magnetic resonance imaging, Nucl. Med. Commun. 32 (8) (2011) 716–723.

[31] D. Beiki, G. Yousefi, B. Fallahi, M.N. Tahmasebi, A. Gholamrezanezhad, A. Fard-Esfahani, M. Erfani, M. Eftekhari, 99m)tc-Ubiquicidin (29-41), a promising radiopharmaceutical to differentiate orthopedic implant infections from sterile inflammation, Iran, J. Pharm. Res. 12 (2) (2013) 347–353.

[32] Q. Yin, L. Tang, K. Cai, R. Tong, R. Sternberg, X. Yang, L.W. Dobrucki, L.B. Borst, D. Kamstock, Z. Song, W.G. Helferich, J. Cheng, T.M. Fan, Pamidronate functionalized nanoconjugates for targeted therapy of focal skeletal malignant osteolysis, Proc. Natl. Acad. Sci. U. S. A. 113 (32) (2016) E4601–E4609.

[33] S. Huo, C. Chen, Z. Lyu, S. Zhang, Y. Wang, B. Nie, B. Yue, Overcoming planktonic and intracellular Staphylococcus aureus-associated infection with a cell-

[34] penetrating peptide-conjugated antimicrobial peptide, ACS Infect. Dis. 6 (12) (2020) 3147–3162.

[34] V.A. Truong, M.N. Hsu, N.T. Kieu Nguyen, M.W. Lin, C.C. Shen, C.Y. Lin, Y.C. Hu, CRISPRai for simultaneous gene activation and inhibition to promote stem cell chondrogenesis and calvarial bone regeneration, Nucleic Acids Res. 47 (13) (2019) e74.

[35] B. Nie, T. Long, H. Ao, J. Zhou, T. Tang, B. Yue, Covalent immobilization of enoxacin onto titanium implant surfaces for inhibiting multiple bacterial species infection and in vivo methicillin-resistant Staphylococcus aureus infection prophylaxis, Antimicrob. Agents Chemother. 61 (1) (2017) e01766–16.

[36] X. Qu, H. Yang, B. Jia, M. Wang, B. Yue, Y. Zheng, K. Dai, Zinc alloy-based bone internal fixation screw with antibacterial and anti-osteolytic properties, Bioact Mater. 6 (12) (2021) 4607–4624.

[37] S. Huo, F. Wang, Z. Lyu, Q. Hong, B.e. Nie, J. Wei, Y. Wang, J. Zhang, B. Yue, Dual-functional polyetheretherketone surface modification for regulating immunity and bone metabolism, Chem. Eng. J. 426 (2021) 130806.

[38] H. Chen, M. Zhang, B. Li, D. Chen, X. Dong, Y. Wang, Y. Gu, Versatile antimicrobial peptide-based ZnO quantum dots for in vivo bacteria diagnosis and treatment with high specificity, Biomaterials 53 (2015) 532–544.

[39] N. Huang, X. Chen, X. Zhu, M. Xu, J. Liu, Ruthenium complexes/polypeptide self-assembled nanoparticles for identification of bacterial infection and targeted antibacterial research, Biomaterials 141 (2017) 296–313.

[40] H. Zhang, T. Fan, W. Chen, Y. Li, B. Wang, Recent advances of two-dimensional materials in smart drug delivery nano-systems, Bioact Mater. 5 (4) (2020) 1071–1086.

[41] P. Pan, Q. Yue, J. Li, M. Gao, X. Yang, Y. Ren, X. Cheng, P. Cui, Y. Deng, Smart cargo delivery system based on mesoporous nanoparticles for bone disease diagnosis and treatment, Adv. Sci. 8 (12) (2021), e2004586.

[42] F. Tang, L. Li, D. Chen, Mesoporous silica nanoparticles: synthesis, biocompatibility and drug delivery, Adv. Mater. 24 (12) (2012) 1504–1534.

[43] W. Zakrzewski, M. Dobrzynski, Z. Rybak, M. Szymonowicz, R.J. Wiglusz, Selected nanomaterials' application enhanced with the use of stem cells in acceleration of alveolar bone regeneration during augmentation process, Nanomaterials 10 (6) (2020) 1216.

[44] G. Qi, L. Li, F. Yu, H. Wang, Vancomycin-modified mesoporous silica nanoparticles for selective recognition and killing of pathogenic gram-positive bacteria over macrophage-like cells, ACS Appl. Mater. Interfaces 5 (21) (2013) 10874–10881.

[45] E.D. Brown, G.D. Wright, Antibacterial drug discovery in the resistance era, Nature 529 (7586) (2016) 336–343.

[46] S.J. Dancer, How antibiotics can make us sick: the less obvious adverse effects of antimicrobial chemotherapy, Lancet Infect. Dis. 4 (10) (2004) 611–619.

[47] S.Y. Tong, J.S. Davis, E. Eichenberger, T.L. Holland, V.G. Fowler Jr., Staphylococcus aureus infections: epidemiology, pathophysiology, clinical manifestations, and management, Clin. Microbiol. Rev. 28 (3) (2015) 603–661.

[48] Z. Li, D.L. Clemens, B.Y. Lee, B.J. Dillon, M.A. Horwitz, J.I. Zink, Mesoporous silica nanoparticles with pH-sensitive nanovalves for delivery of moxifloxacin provide improved treatment of lethal pneumonic tularemia, ACS Nano 9 (11) (2015) 10778–10789.

[49] S. Saeed, J. Zafar, B. Khan, A. Akhtar, S. Qurieshi, S. Fatima, N. Ahmad, J. Irfanullah, Utility of 99mTc-labelled antimicrobial peptide ubiquicidin (29-41) in the diagnosis of diabetic foot infection, Eur. J. Nucl. Med. Mol. Imag. 40 (5) (2013) 737–743.

[50] J.W. Costerton, P.S. Stewart, E.P. Greenberg, Bacterial biofilms: a common cause of persistent infections, Science 284 (5418) (1999) 1318–1322.

[51] K. Zheng, J. Kang, B. Rutkowski, M. Gawęda, J. Zhang, Y. Wang, N. Founier, M. Sitarz, N. Taccardi, A.R. Boccaccini, Toward highly dispersed mesoporous bioactive glass nanoparticles with high Cu concentration using Cu/ascorbic acid complex as precursor, Front. Chem. 7 (2019) 497.

[52] D. Wang, Y. Yao, J. He, X. Zhong, B. Li, S. Rao, H. Yu, S. He, X. Feng, T. Xu, B. Yang, T. Yong, L. Gan, J. Hu, X. Yang, Engineered cell-derived microparticles Bi (2)Se(3)/DOX@MPs for imaging guided synergistic photothermal/low-dose chemotherapy of cancer, Adv. Sci. 7 (3) (2020) 1901293.

[53] F. Foschi, J. Izard, H. Sasaki, V. Sambri, C. Prati, R. Müller, P. Stashenko, Treponema denticola in disseminating endodontic infections, J. Dent. Res. 85 (8) (2006) 761–765.